# Journal of Materials Chemistry A

Accepted Manuscript


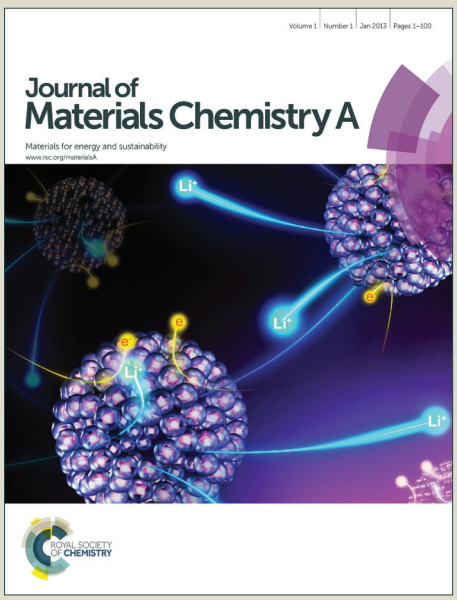





ROYAL SOCIETY OF CHEMISTRY

www.rsc.org/materialsA

# Large-scale synthesis of Ag-Si core-shell nanowall arrays as high-performance anode materials of Li-ion batteries

Wenjia Zhao, Ning Du, Chengmao Xiao, Hao Wu, Hui Zhang, Deren Yang*

**Abstract**

We demonstrate the synthesis of Ag-Si core-shell nanowall arrays via a simple displacement reaction and subsequent RF-sputtering deposition. The displacement between Cu substrate and $Ag^+$ leads to Ag nanowall arrays with good substrate adhesion. The Ag nanowall arrays can function as a mechanical support and an efficient electron conducting pathway for Si anode materials. These Ag-Si core-shell nanowall arrays show the discharge capacity >1500 mAh $g^{-1}$ at a current density of 2100 mA $g^{-1}$ after 400 cycles. The capacity fade from 2$^{nd}$ to 400$^{th}$ cycles is only 0.1 % per cycle. Moreover, the cycling performance can be retained when the thickness of the Si layer increases, clearly demonstrating the superior cycling performance of Ag-Si core-shell nanowall arrays. Considering the simple and large-scale synthesis of Ag-Si core-shell nanowall arrays, this work may facilitate the commercial application of Si anode materials for Li-ion batteries.

**Introduction**

Silicon (Si) is a promising anode material of lithium-ion batteries (LIBs) due to its high theoretic capacity ( ~4200 $mAhg^{-1}$) and relatively low working potential (0.37mV *vs* $Li/Li^+$), which is considered to be a potential alternative for commercial graphite [1-3]. However, the large volume changes (>400%) that occur during lithium insertion and extraction leads to cracking and crumbling of the electrode, which in turn causes capacity fades and poor cycling life [4-6].To solve this issue, Si nanostructures[7-9], Si porous structures [10-12] and Si-based composites [13-18] have been studied. The previous results show some improvements over existing Si anode, but only to a limited extent. For example, Yi Cui's group demonstrated the growth of Si nanowires on a current collector as anode of LIBs [7]. Si nanowires can

*Author to whom correspondence should be addressed; electronic mail: mseyang@zju.edu.cn, tel: 86-571-87953190, fax: 86-571-87952322.

accommodate the volume change and enhance the adhesion between the active materials and the current collector, thus obtain the great improvement in cycling performance. However, the complete lithiation of Si nanowires impedes charge transport in the longitudinal direction, which limits the rate performance. Yao et al. prepared Si-PPy-Ag composites by chemical polymerization of pyrrole, $AgNO_3$ and nanosilicon powder as anode materials of LIBs [18]. However, the capacity decay can't be prevented and a capacity of ~800 $mAhg^{-1}$ was obtained after 100 cycles, indicating that simple blend of Si, Ag and carbon source is not fully satisfied. Du et al. synthesized graphene-wrapped silver-porous silicon composite via magnesiothermic reduction, silver-mirror reaction, and blend with graphite oxide and thermal reduction. In this case, the synthetic process is relatively complicated and the addition of graphene is necessary for the improved cycling performance of Si anode. To simultaneously obtain the high capacity, good cycling life and rate capability remains a great challenge.

Recently, Si-based inactive/active composite structures have attracted great attention because the inactive component can act as a mechanical support and an efficient electron conducting pathway during the charge/discharge process, which can enhance the cycling and rate performance [19-26]. As a result, carbon/Si [19],c-Si/a-Si [20], $TiSi_2$/Si [21], $Ni_xSi_y$/Si [22], Ni/Si [23-25], Cu/Si [25], Co/Si [26] core-shell structures have been synthesized and investigated as anode for LIBs. The Si layer can be easily achieved by either chemical vapor deposition and sputtering methods. In contrast, the core or inactive component represents the most important part that is difficult to achieve. However, the previous methods such as the chemical vapor deposition (CVD) and electrochemical growth of the inactive component seems relatively sophisticated, expensive and some of them need strict voltage control, which is not practical for commercial LIBs. For example, Cu/Si core-shell nanowires exhibited the good cycling performance, while the Cu nanowire arrays were synthesized via a sophisticated nanoporous membrane-assisted method [25]. The sophisticated synthetic procedure limits its further application.

Results and discussion

Herein, we use a simple displacement reaction to obtain Ag nanowall arrays on Cu substrate, which can act as a mechanical support as well as an efficient electron conducting pathway to enhance the cycling and rate performance for Si anodes. **Figure 1** shows the schematic illustration for the synthesis of Ag nanowall arrays on a Cu substrate. A fresh Cu substrate was simply immersed in the silver nitrate ($AgNO_3$) solution to obtain the Ag nanowall arrays on the surface of the Cu substrate. After the substitution reaction, the surface of the Cu substrate turns from brass to silver color, indicating the deposition of Ag. **Figure 2** shows the morphological and compositional characterization of Ag nanowall arrays on a Cu substrate. As can be seen, the as-synthesized Ag show the morphology of nanowalls with the width from several hundred nanometers to several micrometers and the thickness of ~100 nm, which is aligned vertically on the substrate. The Ag nanowall arrays may be attributed to non-equilibrium and anisotropic growth from the displacement reaction between Cu and $Ag^+$ [27], however, the detailed growth mechanism should be further investigated. The Ag nanowall arrays can be obtained with $AgNO_3$ solution in a certain concentration range. In a series of continuous experiments, we can supply $AgNO_3$ to the original solution to maintain the concentration to a certain range, which can make full use of $AgNO_3$. Moreover, the Ag nanowalls show strong adhesion with the Cu substrate due to the displacement reaction. The strong adhesion of the Ag nanowall arrays with the substrate could facilitate the cycling performance of Si anode. **Figure 2c** shows the TEM image of an individual Ag nanowall scrapped from the substrate. As can be seen, the size of the Ag nanowall is about 1 μm. In the HRTEM image (**Figure 2d**), the marked planes correspond to the {111} and {200} planes of Ag, further indicating to the synthesis of Ag nanowalls. After the deposition of Si layer for 40 min, the thickness of the nanowalls significantly increases 300~500 nm (**Figures 3a and b**). The array structures have been totally retained after the RF-deposition. **Figure 3c** shows the STEM image of an individual Ag-Si nanowall. It can be seen that the Si layer has been deposited onto the whole Ag nano-plate, while the thickness decreases gradually from the top to the bottom, which is the characteristic of the RF-sputtering. The corresponding line-scan EDX patterns further confirm the

variation of the thickness of Si layer along the Ag nanowall (**Figure 3d**). Considering Ag can alloy with Li, the effective mass is the sum of Ag and Si for the calculation of capacity. When the deposition time is 40 min, the mass ratio of Si to Ag is about 1.5. Figure 3e shows the TEM and HRTEM (inset) images of an individual Ag-Si nanowall. It can be seen that an amorphous Si layer has been deposited onto the crystalline Ag nanowall, and the lattice spacing of 0.236 nm corresponds to the {111} plane of Ag. The XRD pattern (Figure 3f) indicates that only the peaks of Cu and Ag can be detected, further confirming the crystalline Ag nanowall has grown on the Cu substrate and the coated Si layer is amorphous.

Motivated by the novel core-shell nano-wall array structures, the products were tested as anode of LIBs. **Figure 4a** shows the first three CV curves of Ag-Si core-shell nanowall arrays (CNAs) in the potential range of 0 ~1.2 V at a scan rate of 0.1 $mVs^{-1}$. In the first cycle, there was a broad cathodic peak located at 0.18 V, which disappeared in the subsequent cycles. This peak can be assigned to the formation of a solid electrolyte interphase (SEI) film [24]. Other peaks located between 0 and 0.4 V is attributed to theformation of Li-Si alloys [28]. In the anodic process, the peaks at 0.35 and 0.5 V can be assigned to the phase transition between $Li_xSi$ and Si [28]. After the first cycle, the CV curves tend to be stable and nearly overlap, indicating the good cycling performance in the following cycles. There is no peaks related with the reaction between Ag and Li can be detected [29-30], which may be due to the relatively low contribution of the Ag in the Ag-Si CNA. The capacity contribution of Ag in the Ag-Si CNAs is between 10 % ($1^{st}$cycle)~2 % ($200^{th}$ cycle) in the 200 cycles, which can be ignored to some extent in the following discussion. The contribution of Ag in the Ag-Si CNAs decreases because the capacity of Ag fades faster than Si. **Figure 4b** shows the $1^{st}$, $2^{nd}$, $3^{rd}$ and $100^{th}$ discharge/charge curves of the Ag-Si CNAs at a current density of 2100 $mAg^{-1}$ (0.5 C). It can be seen that the first discharge and charge capacity is 3899 and 2629 $mAhg^{-1}$, respectively, indicating the initial coulombic efficiency of 67.4%. The relatively low initial coulombic efficiency may be due to the formation of SEI film and the existence of silicon oxide. The existence of silicon dioxide is due to the residual oxygen in our sputtering system [22]. The

initial coulombic efficiency can be improved by upgrading the vacuum system. From the 2nd cycle, the discharge capacity decreases slowly. The discharge capacity of 100th cycle is 2136 $mAhg^{-1}$, which is nearly 5 times larger than the theoretic capacity of the commercial graphite anode. **Figure 4c** shows the discharge and charge capacity, and the coulombic efficiency versus cycle number for the Ag-Si CNAs at a current density of 0.5 C (2100 $mAg^{-1}$). It can be seen that the coulombic efficiency is higher than 90% after the first cycle, and increase to higher than 95% after 5 cycles. The discharge capacity of the second cycle is 2750 $mAhg^{-1}$, which decreases slowly in the subsequent cycles. After 400 cycles, the discharge capacity is 1679 $mAhg^{-1}$, indicating 61% retention of initial reversible capacity. This means that only an average of 0.1 % capacity fade per cycle was observed between the 2nd and 400 cycles, which is better than comparable data reported in literature [19-25]. **Figure 4d** shows the cycling performance for the Ag-Si CNAs at different current densities. As observed, the discharge capacity at 0.2 C is ~2200 $mAhg^{-1}$, and it drops to 2000, 1960, 1900 and 1820 $mAhg^{-1}$ while the current density increases to 0.5, 1, 2 and 5 C, respectively. Even at a high current density of 10 C (42 $Ag^{-1}$), the capacity can be maintained at 1500 $mAhg^{-1}$, indicating the superior rate performance of the Ag-Si CNAs. When the current density recovers to 0.2 C, the capacity is ~2000 $mAhg^{-1}$, further confirming the good rate performance of the Ag-Si CNAs. For comparison, the Si nanowires show a higher discharge capacity than the Ag-Si CNAs at low current density (0.2 C) [7]. However, at higher current densities, the Ag-Si CNAs show significantly higher capacity retention. The capacity of the Ag-Si CNAs surpasses the Si nanowires in the case of higher than 1 C, indicating the better rate capability of the Ag-Si CNAs. As mentioned above, the complete lithiation of Si nanowires impedes charge transport in the longitudinal direction, which limits the rate performance of Si nanowires. Herein, the core-shell array structures should be responsible for the better rate performance. The Ag cores can function as a mechanical support and an efficient electron conducting pathway, which can enhance the stability and conductivity for Si anode. Moreover, the displacement between Cu substrate and $Ag^+$ leads to Ag nanowall arrays with good substrate adhesion, which can also enhance stability of Si anode

during the charge/discharge process.

It is important to provide sufficient active material per unit area to obtain high energy density. However, the traditional Si film anodes suffer from the stress-induced cracking and high inherent resistance along with the increased thickness, which leads to poor cycling and rate performance [31]. Therefore, it is necessary to investigate the cycling performance of Ag-Si CNAs with different thickness of the Si layer. **Figure 5** shows the SEM image of the Ag-Si CNAs with different deposition time of Si and the corresponding discharge capacity versus cycle numbers. It can be seen that the thickness of Si layer increases apparently along with the increased deposition time. When the deposition time increases to 80 min (**Figure 5c**), the Si layer has almost covered the entire area, indicating that it has more active materials per area than that with 20 (**Figure 5a**) and 60 (**Figure 5b**) min deposition. In detail, the quality per unit area of Si with 80 min deposition is about 2.6 times of that with 40 min deposition. It should be mentioned that the mass ratio of Ag is only ~16 % in the Ag-Si CNAs with 80 min deposition, which is desireable to keep this technique cost effective. **Figure 5d** shows the discharge capacity versus cycle numbers of Ag-Si CNAs with three different thicknesses of the Si layer. It can be seen that the three anodes show similar cycling performance. This result means that the thick Si layer show a similar cycling performance compared to thin Si layer, with the use of the Ag-Si CNAs scheme.

To confirm the advantage of the Ag-Si CNA anode, the cycling performance of the Si film anode was compared to plane Si anode (**Figure 6a**). It can be seen that the plane anode shows a similar initial reversible capacity with the CNA anode, while the capacity of the plane anode decreases rapidly to nearly 100 $mAhg^{-1}$ after 40 cycles. For comparison, the CNA anode shows a stable capacity of ~2000 $mAhg^{-1}$ during 40 cycles. As mentioned earlier, the Ag nanoarray cores can function as a mechanical support as well as an efficient electron conducting pathway for Si anode materials, and thus can enhance their cycling performance. **Figure 6b** shows the AC impedance measurements for the CNA and plane anodes after 5 cycles, respectively. It can be seen that both spectra consist of a depressed semicircle in the high-medium frequency range and a straight line in the low frequency range. At high frequencies, the spectrum

is dominated by external cell connections, electrical conduction between the current collector and sputtered substance, and the ionic conduction through the electrolyte [32]. As the frequency decreased to high-medium range, the depressed semicircle in the spectrum is attributed to the interfacial charge transfer impedance and SEI film [33]. And in the low frequency range, the straight line can be attributed to the diffusion of Li in the electrodes [34].As observed, the diameter of the semicircle in the CNA anode is significantly smaller than that of the plane anode, revealing lower charge-transfer impedances. This result confirms that the Ag nanoarray core can act as an efficient electron conducting pathway to enhance the conductivity of Si anode. To verify the stability of the CNA anode during the charge/discharge process, the morphology of the CNA and plane anodes after cycling has been investigated (**Figures 6c and d**). As observed, the morphology of the CNA anode has been mainly retained, while the plane anode seems to crack and even loses contact with the current collector. Therefore, we can conclude that the Ag nanoarray cores can enhance the stability of the Si anode during the charge/discharge process.

The Ag nanowall arrays can not only support Si, but also other anode materials to enhance their performance. **Figure 7** shows the Ag nanowall array-supported Ge and $Co_3O_4$ materials and their corresponding cycling performance. It can be seen that the Ge and $Co_3O_4$ can also be deposited onto Ag nanowall arrays by RF-sputtering process (**Figures 7a and c**). The as-synthesized Ag-Ge and Ag-$Co_3O_4$CNA anodesshowan enhanced cycling performance compared to thecorresponding plane anodes (**Figures 7b and d**). Similar to the Ag-Si CNA anode, the core-shell array structures is likely responsible for the enhanced cycling performance.

## Conclusions

Ag-Si core-shell nanowall arrays were synthesized via a simple displacement reaction and subsequent deposition of Si layer. When used as anode of LIBs, the Ag-Si core-shell nanowall arrays show the discharge capacity >1500 mAh $g^{-1}$ at a current density of 2.1A $g^{-1}$ after 400 cycles. The capacity fade from 2$^{nd}$ to the 400$^{th}$ cycles is only 0.1 % per cycle. Even at a high current density of 41 A $g^{-1}$, the capacity

can be maintained at ~1500 $mAhg^{-1}$. The Ag cores can function as a mechanical support and an efficient electron conducting pathway, which can enhance the stability and conductivity for Si anode during the charge/discharge process. Such the strategy can be extended to other anode materials to enhance their cycling performance.

## Experimental section

*Synthesis of Ag-Si core-shell nanowall arrays on a Cu substrate*

Copper substrate with the thickness of 0.1mm was first cut into 1.6cm×1.6cm slices, and then flattened and washed with deionized water and ethanol. Ag nanowall arrays were synthesized by immersing the Cu substrate into $AgNO_3$ (99.9999%, Adrich) solution (5 mM) for 30 s. The as-prepared samples were quickly taken out from the solution, and washed with deionized water and ethanol for several times, finally dried in vacuum oven. A Si layer was deposited on the as-prepared substrate by radio frequency magnetron sputtering using a Si target. The sputtering was done at a working pressure of 2 Pa at 20°C, and the power was 80 W. The sputtering time was 40min. When the deposition time increase from 20 to 40, 60 and 80 min, the mass per unit area of Si is 0.9, 1.9, 3.7 and 4.8 $*10^{-2}$ mg $cm^{-2}$, respectively, while the mass per unit area of Ag is maintained at 0.8 $*10^{-2}$ mg $cm^{-2}$.

*Synthesis of Ag-Ge, Ag-$Co_3O_4$ core-shell nanowall arrays on a Cu substrate*

The synthetic procedure of the Ag nanowall arrays is the same as the above-mentioned. For Ag-$Co_3O_4$ core-shell nanowall arrays, a $Co_3O_4$ layer was deposited with the same working conditions as Si for 40min. For Ag-Ge core-shell nanowall arrays, a Ge layer was deposited at a working pressure of 1 Pa, and the power was 100 W for 10 min.

*Characterization and electrochemical measurement*

The morphology and structure of the samples were examined by a field emission scanning electron microscope (SEM HITACH S4800) with an energy-dispersive X-ray spectrometer (EDX) and a transmission electron microscope (TEM FEI F20).

Electrochemical measurements were performed by coin type cells (CR2025) which were assembled in a glove box (MBRAUN, LABstar, Germany) under an argon

atmosphere by directly using the as-synthesized samples as the anodes. The counter electrode was lithium metal foil (15 mm in diameter), and the electrolyte solution was 1M solution of $LiPF_6$ in ethylene carbonate (EC) and Dimethyl carbonate (DMC) (1:1 by volume). Finally, the cells were then aged for 12h before measurements. A galvanostatic cycling test of the assembled cells was carried out on a Land CT2001A system within the potential range of 0.01~1.2 V at various discharge/charge current densities for Ag-Si anodes. Ag-Ge was tested within the same potential range, while Ag-$Co_3O_4$ was tested within the potential range of 0.01~3 V. Cyclic voltammetry (CV) was conducted in the potential window of 0.01~1.2 V and a scan rate of 0.1 mV $s^{-1}$ on an Arbin BT 2000 system. After five cycles, electrochemical impedance spectroscopy (EIS) measurements were performed using electrochemical workstation (Shanghai Chenhua Instrument Co., China). For the calculation of the capacity, the effective mass of the active materials is the sum of Ag and Si. The effective mass is the sum of Ag and Si. From the reaction ($2Ag^{+}+Cu \rightarrow 2Ag+Cu^{2+}$ ) we can conclude that the increased mass is due to the deposition of 2 copies of Ag and the release of 1 copies of Cu. Therefore, the effective mass of Ag is about 216/(216-64)*(the increased mass). The effective of Si can be simply measured by the increased mass after RF-deposition, therefore, the total effective mass of Ag and Si can be calculated.

**Acknowledgement**

The authors would like to appreciate the financial supports from the 863 Project (No. 2011AA050517), Natural Science Foundation of China (No. 51002133), Zhejiang Provincial Natural Science Foundation of China (LY13E020003) and the Fundamental Research Funds for the Central Universities.

**Notes and references**

*State Key Lab of Silicon Materials and Department of Materials Science and Engineering, Cyrus Tang Center for Sensor Materials and Applications, Zhejiang University, Hangzhou 310027, People's Republic of China*

*Email:mseyang@zju.edu.cn*

[1] B. A. Boukamp, G. C. Lesh, R. A. Huggins, *J. Electrochem. Soc.* **1981**, *128*, 725.

[2] M. Winter, J. O. Besenhard, M. E. Spahr, P. Novak, *Adv. Mater.* **1998**, *725*, 10.

[3] S. Ohara, J. Suzuki, K. Sekine, T. Takamura, *J. Power Sources* **2003**, *591*, 119.

[4] L. Y. Beaulieu, T. D.Hatchard, A. Bonakdarpour, M. D. Fleischauer, J. R. Dahn, *J. Electrochem. Soc.* **2003**, *150*, A1457.

[5] T. D. Hatchard, J. R. Dahn, *J. Electrochem. Soc.* **2004**, *151*, A838.

[6] S. Golmon, K. Maute, S-H. Lee, M. L. Dunn, *Appl. Phys. Lett.* **2010**, *97*, 033111.

[7] C. K. Chan, H. L. Peng, G. Liu, K. Mcilweath, X. F. Zhang, R. A. Huggins, Y. Cui, *Nat. Nanotech.* **2008**, *3*, 31.

[8] T. Song, J. Xia, J. Lee, D. Lee, M. Kwon, J. Choi, J. Wu, S. Doo, H. Chang, W. Park, D. Zang, H. Kim, Y. Huang, K. Hwang, J. Rogers, U. Paik, *Nano Lett.* **2010**, *10*, 1710.

[9] M. Park, M. Kim, J. Joo, K. Kim, J. Kim, S. Ahn, Y. Cui, J. Cho, *Nano Lett.* **2009**, *9*, 3844.

[10] H. Kim, B. Han, J. Choo, J. Cho, *Angew. Chem. Int. Ed.* **2008**, *47*, 10151.

[11] B. Bang, H. Kim, H. Song, J. Cho and S. Park, *Energy Environ. Sci.* **2011**, *4*, 5013.

[12] C. Du, C. Gao, G. Yin, M. Chen and L. Wang, *Energy Environ. Sci.* **2011**, *4*, 1037.

[13] B. Kim, H. Uono, T. Satou, T. Fuse, T. Ishihara, M. Ue, M. Senna, *J. Electrochem. Soc.* **2005**, *152*, A523.

[14] Y. Zhang, X. Zhang, H. Zhang, Z. Zhao, F. Li, C. Liu, H. Cheng, *Electrochim. Acta* **2006**, *51*, 4994.

[15] N. Dimov, S. Kugino, A. Yoshio, *J. Power Sources* **2004**, *136*, 108.

[16] Y. Liu, B. Chen, F. Cao, H. Chan, X. Zhao, J. Yuan, *J. Mater. Chem.* **2011**, *21*, 17083.

[17] F. Du, K. Wang, W. Fu, P. Gao, J. Wang, J. Yang, J. Chen, *J. Mater. Chem.* **2013**, *1*, 13648.

[18] J. Yao, Z. Jia, P. Zhang, C. Shen, J. Wang, K. Aguey-Zinsou, L. Wang, *Ionics* **2013**, *19*, 401.

[19] L. Cui, Y. Yang, C. Hsu, Y. Cui, *Nano Lett.* **2009**, *9*, 3370.

[20] L. Cui, R. Ruffo, C. Chan, H. Peng, Y. Cui, *Nano Lett.* **2009**, *9*, 491.

[21] S. Zhou, X. Liu, D. Wang, *Nano Lett.* **2010**, *10*, 860.

[22] N. Du, X. Fan, J. Yu, H. Zhang, D. Yang, *Electrochem. Commun.* **2011**, *13*, 1443.

[23] X. Chen, K. Gerasopoulos, J. Guo, A. Brown, C. Wang, R. Ghodssi, J. Culver, *ACS Nano* **2010**, *4*, 5366.

[24] S. Zhang, Z. Du, R. Lin, T. Jiang, G. Liu, X. Wu, D. Weng, *Adv. Mater.* **2010**, *22*, 5378.

[25] J. Qu, H. Li, J. Henry Jr., S. Martha, N. Dudney, H. Xu, M. Chi, M. Lance, S. Mahurin, T. Besmann, S. Dai, *J. Power Sources* **2012**, *198*, 312.

[26] Y. Tang, X. Xia, Y. Yu, S. Shi, J. Chen, Y. Zhang, J. Tu, *Electrochimica Acta* **2013**, *88*, 664.

[27] H. Xia, S. Tang, L. Lu, *Mater. Res. Bull.* **2007**, *42*, 1301.

[28] L. Chen, J. Xie, H. Yu, T. Wang, *J. Appl. Electrochem.* **2009**, *39*, 1157.

[29] G. Taillades, J. Sarradin, *J. Power Sources* **2004**, *125*, 199.

[30] J. Morales, L. Sanchez, F. Martin, J. Ramos-Barrado, M. Sanchez, *J. Electrochem. Soc.* **2004**, *151*, A151.

[31] U. Kasavajjula, C. Wang, A. Appleby, *J. Power Sources* **2007**, *163*, 1003.

[32] G. Wang, Z. Lu, X. Gao, X. Liu, J. Wang, *J. Power Sources* **2009**, *189*, 655.

[33] R. Ruffo, S. Hong, C. Chan, R. Huggins, Y. Cui, *J. Phys. Chem. C* **2009**, *113*, 11390.

[34] C. Wang, A. Appleby, F. Little, *J. Electroanal. Chem.* **2001**, *497*, 33.

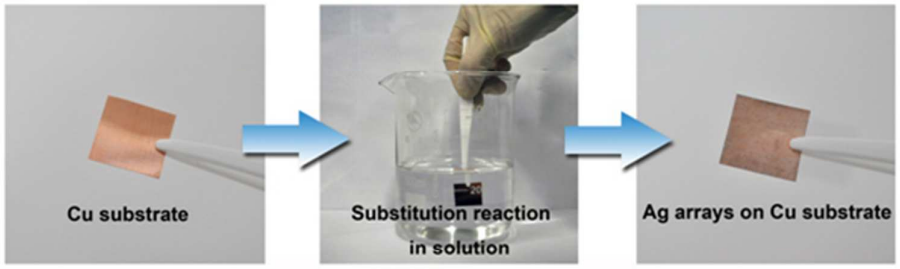


**Figure 1.**Schematic of the fabrication process for the Ag nanowall arrays on a Cu substrate.

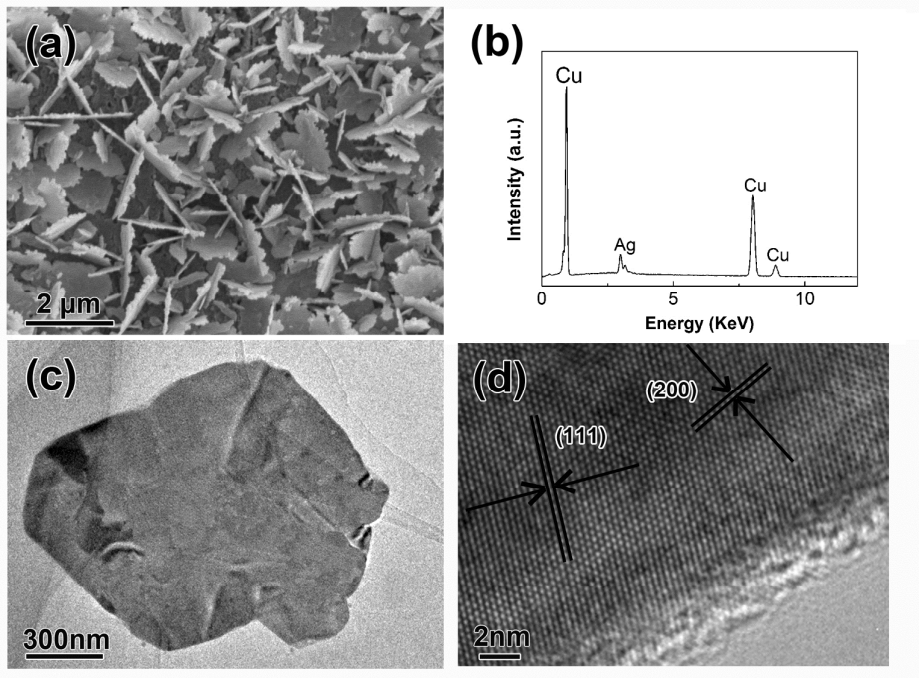


**Figure 2.**SEM images (a), EDX spectrum (b), TEM image (c) and HRTEM image (d) of the Ag nanowall arrays on a Cu substrate.

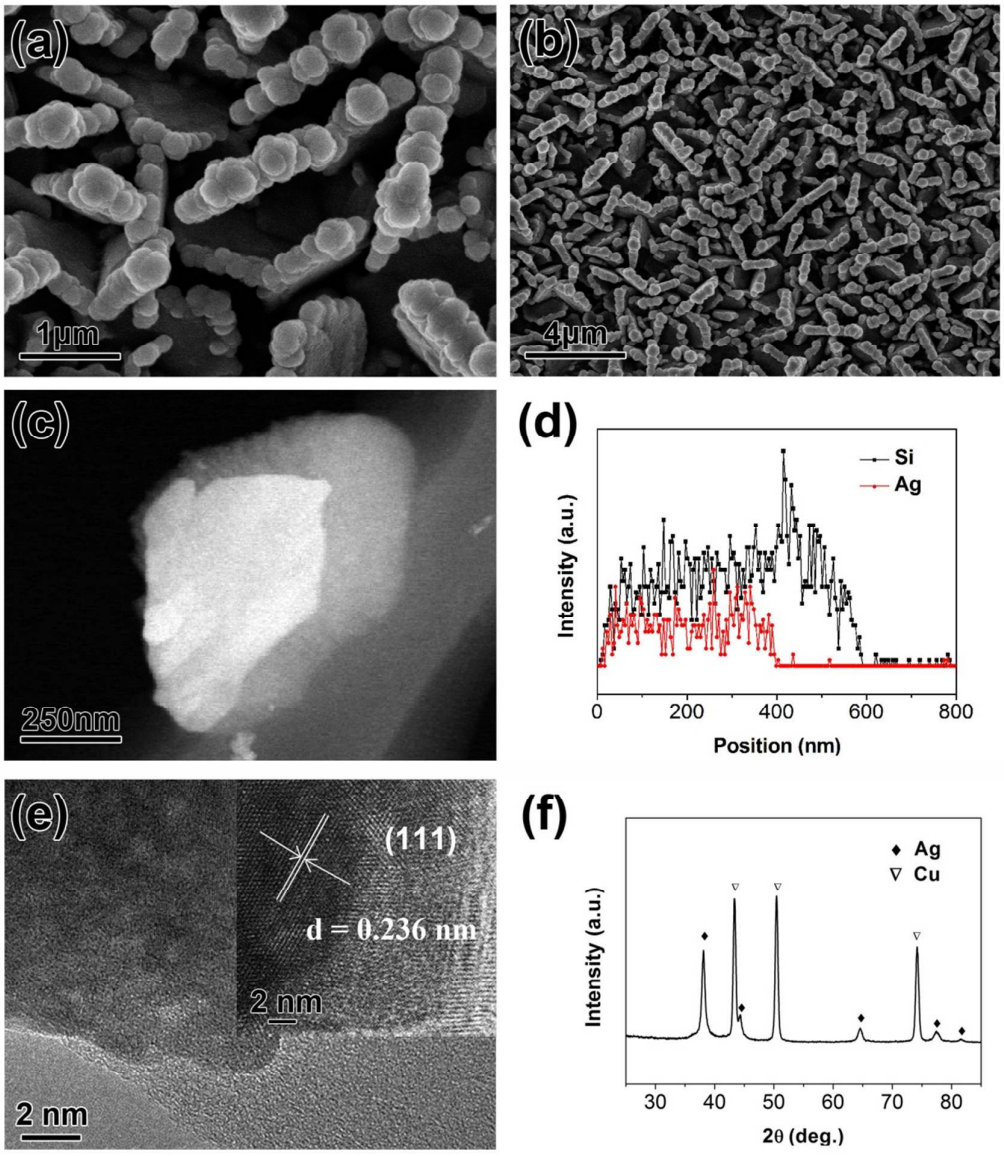


**Figure 3.** SEM images (a) and (b), STEM image (c), compositional line profile across the nanowall probed by EDX spectroscopy(d), TEM image (inset HRTEM image) (e) and XRD pattern (f) of the Ag-Si CNAs on the Cu substrate.

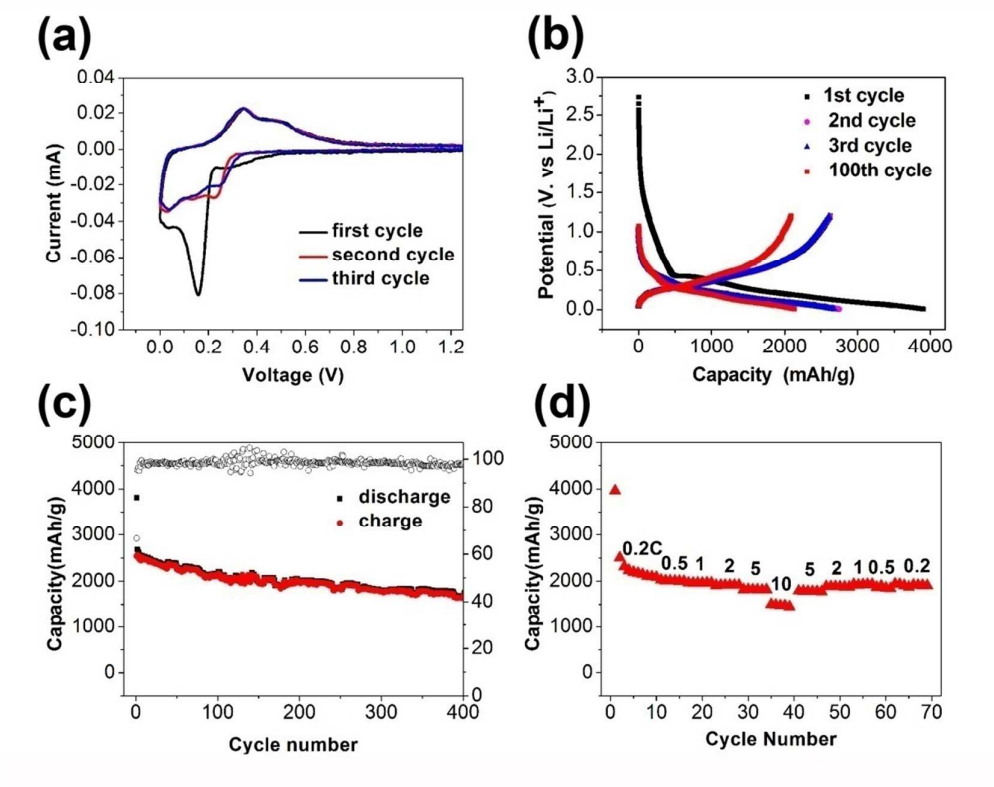


**Figure 4.**(a) The first three CV curves of the Ag-Si CNAs in the potential range of 0.0-1.2V at a scan rate of 0.1 $mVs^{-1}$; (b) the $1^{st}$, $2^{nd}$, $3^{rd}$ and $100^{th}$ discharge-charge curves of the Ag-Si CNAs at a current density of 2100 $mAg^{-1}$ at room temperature;(c) discharge and charge capacities versus cycle number for the Ag-Si CNAs; (d) cycling performance at various C rates of the Ag-Si CNAs.

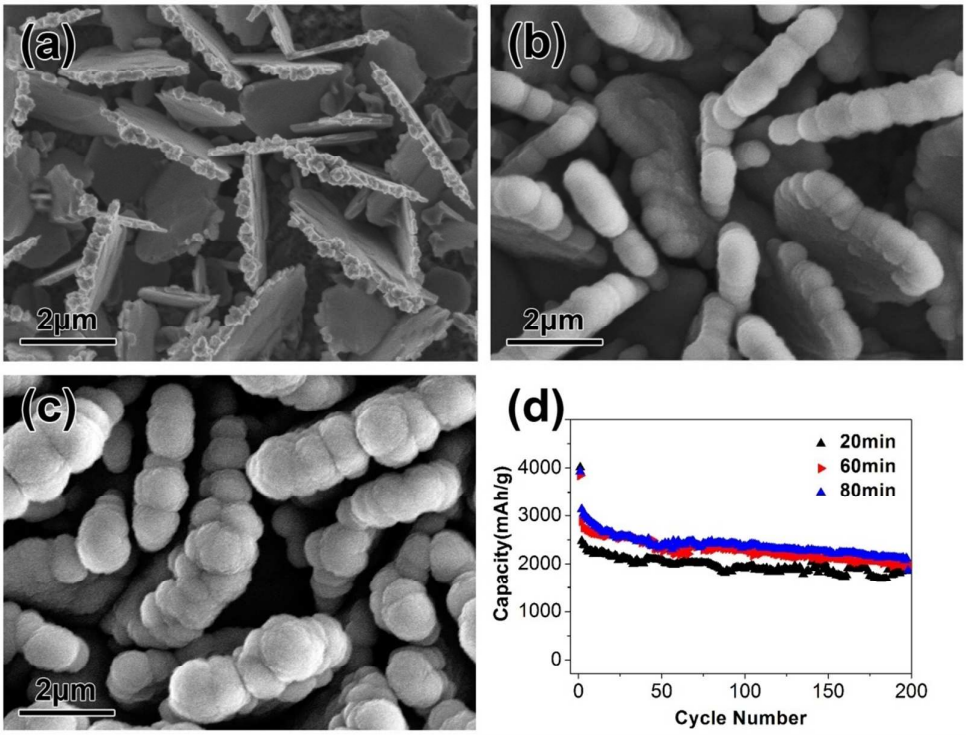


**Figure 5.**SEM images of the Ag-Si CNAs with different deposition time of Si layer: (a) 20 min; (b) 60 min; (c) 80 min, respectively; (d) their corresponding discharge capacities versus cycle numbers at a current density of 2100 $mAg^{-1}$.

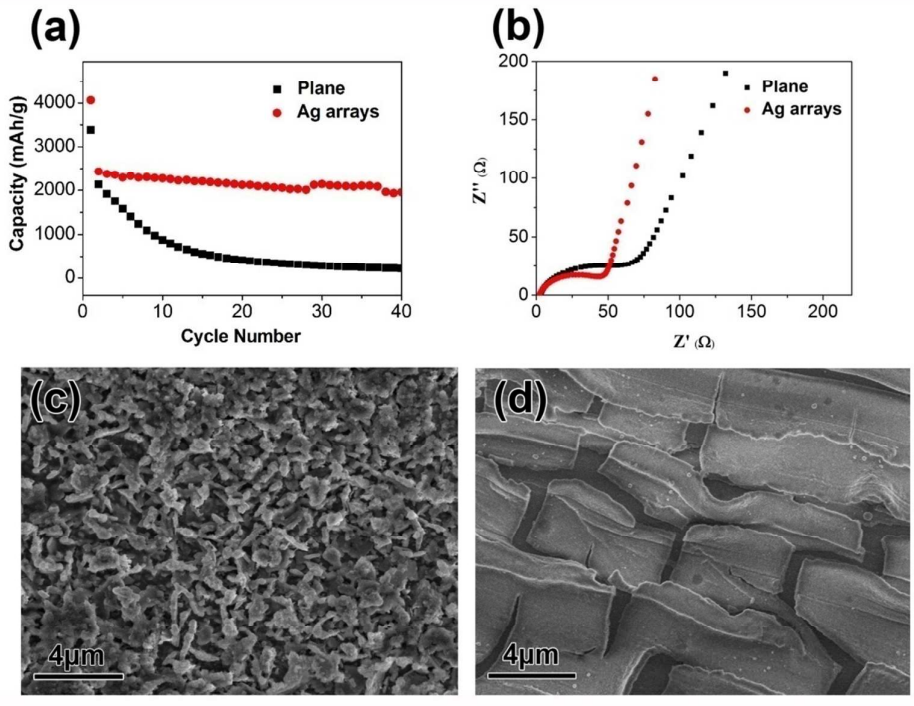


**Figure 6.** (a) cycling performance for the Ag-Si CNAs and planer electrodes at the current density of 2100 $mAg^{-1}$, respectively; (b) Nyquist plots of the Ag-Si CNAs and planer electrodes obtained by applying a sine wave with amplitude of 5 mV over the frequency range 100 kHz to 0.01 Hz; (c) SEM image of a Ag-Si CNA anode after cycling; (d) SEM image of a plane Si anode after cycling.

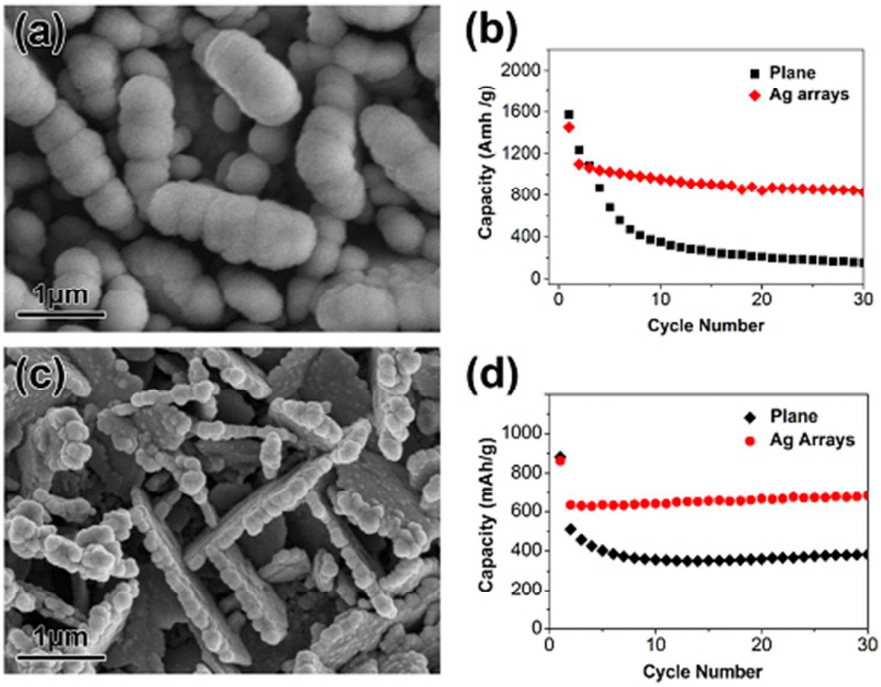


**Figure 7** (a) SEM image of the Ag-Ge CNAs; (b) cycling performance of the Ag-Ge CNAs and plane Ge anodes; (c) SEM image of the Ag-$Co_3O_4$ CNAs; (d) cycling performance of the Ag- $Co_3O_4$CNAs and plane $Co_3O_4$ anodes.